

Finite element analysis of magnetostrictive energy harvesting concept device utilizing thermodynamic magneto-mechanical model

*Original*

Finite element analysis of magnetostrictive energy harvesting concept device utilizing thermodynamic magneto-mechanical model / Ahmed, U.; Jeronen, J.; Zucca, M.; Palumbo, S.; Rasilo, P.. - In: JOURNAL OF MAGNETISM AND MAGNETIC MATERIALS. - ISSN 0304-8853. - ELETTRONICO. - 486:(2019), p. 165275. [10.1016/j.jmmm.2019.165275]

*Availability:*

This version is available at: 11583/2734639 since: 2019-06-12T09:12:25Z

*Publisher:*

Elsevier

*Published*

DOI:10.1016/j.jmmm.2019.165275

*Terms of use:*

This article is made available under terms and conditions as specified in the corresponding bibliographic description in the repository

*Publisher copyright*

Elsevier postprint/Author's Accepted Manuscript

© 2019. This manuscript version is made available under the CC-BY-NC-ND 4.0 license  
<http://creativecommons.org/licenses/by-nc-nd/4.0/>. The final authenticated version is available online at:  
<http://dx.doi.org/10.1016/j.jmmm.2019.165275>

(Article begins on next page)

## Accepted Manuscript

Finite element analysis of magnetostrictive energy harvesting concept device utilizing thermodynamic magneto-mechanical model

U. Ahmed, J. Jeronen, M. Zucca, S. Palumbo, P. Rasilo

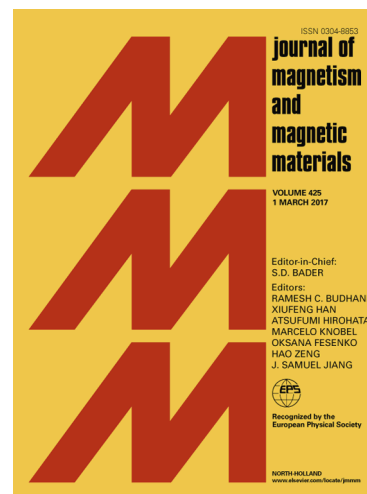
PII: S0304-8853(19)30351-8  
DOI: <https://doi.org/10.1016/j.jmmm.2019.165275>  
Article Number: 165275  
Reference: MAGMA 165275

To appear in: *Journal of Magnetism and Magnetic Materials*

Received Date: 28 January 2019  
Revised Date: 21 March 2019  
Accepted Date: 3 May 2019

Please cite this article as: U. Ahmed, J. Jeronen, M. Zucca, S. Palumbo, P. Rasilo, Finite element analysis of magnetostrictive energy harvesting concept device utilizing thermodynamic magneto-mechanical model, *Journal of Magnetism and Magnetic Materials* (2019), doi: <https://doi.org/10.1016/j.jmmm.2019.165275>

This is a PDF file of an unedited manuscript that has been accepted for publication. As a service to our customers we are providing this early version of the manuscript. The manuscript will undergo copyediting, typesetting, and review of the resulting proof before it is published in its final form. Please note that during the production process errors may be discovered which could affect the content, and all legal disclaimers that apply to the journal pertain.



## Research articles

# Finite element analysis of magnetostrictive energy harvesting concept device utilizing thermodynamic magneto-mechanical model

U. Ahmed<sup>a\*</sup>, J. Jeronen<sup>a</sup>, M. Zucca<sup>b</sup>, S. Palumbo<sup>b, c</sup>, P. Rasilo<sup>a</sup>

<sup>a</sup> Tampere University, Electrical Engineering, P.O. Box 692, FI-33720, Tampere, Finland

<sup>b</sup> Istituto Nazionale di Ricerca Metrologica, INRIM, Metrology for Quality of Life Dept, Strada delle Cacce 91, Torino, Italy

<sup>c</sup> Politecnico di Torino, Dipartimento di Elettronica e Telecomunicazioni, Corso Duca degli Abruzzi 24, Torino, Italy

## ARTICLE INFO

*Keywords:*

Energy harvesting  
Finite element analysis  
Helmholtz free energy  
Magneto-elasticity  
Magnetostrictive devices

## ABSTRACT

This paper utilizes a thermodynamic approach based on Helmholtz free energy density and a finite element (FE) model to analyze a galfenol-based magnetostrictive energy harvesting concept device. An analytical energy density function is first presented assuming an isotropic material for the identification of a magneto-mechanical constitutive law. The model utilizes the magnetic flux density and mechanical strain as state variables. Compared to some earlier approaches, this simplifies the implementation of FE models based on magnetic vector potential and mechanical displacement, since time-consuming inversion of the constitutive law is not required. The Maxwell and mechanical balance equations are then solved utilizing the constitutive law in an axisymmetric FE model. A prototype device is developed and tested under uniaxial cyclic compressive loading of 100 Hz at different preload and dynamic loading cases. Finally, the results from the simulations are compared with the experimental results for validation. The comparison shows that the analytical constitutive model fits well to the magnetization curves measured under static loading. Furthermore, the FE model closely predicts the measured power with some discrepancies under different preload values. The model is able to predict the behavior of the device with respect to preload, load resistance and magnetization of the sample, proving to be an effective tool in the design of such devices.

## 1. Introduction

Magneto-mechanical energy harvesting based on giant magnetostrictive materials (GMMs), e.g. galfenol, Terfenol-D and Metglas, has received increased attention during the past few years, allowing maintenance and battery-free applications. GMMs offer large magnetostrains, strong magneto-mechanical coupling and high operational frequency bandwidth as compared to iron and other ferromagnetic alloys such as nickel and cobalt [1]. The discovery of GMMs has offered their successful incorporation as an active material in various applications including active vibration control, torque sensors and transducers as well as energy harvesters for structural condition monitoring [1], [2]. Mechanical kinetic energy harvesters utilize ambient vibration sources otherwise wasted, originating from, long span bridges, skyscrapers and machines with rotating parts among others, to power up small-scale wireless sensors and transducers.

The effect of magnetostriction is defined as a change in the length or shape of the magnetostrictive material upon magnetization. This phenomenon induces strain in the material

which is due to the fact that randomly aligned magnetic domains tend to align themselves in the direction parallel to the applied magnetic field [3]. The energy harvesters utilize the inverse magnetostrictive effect, which implies change in the magnetic permeability of the material upon mechanical stress, also known as the Villari effect [4]. The application of mechanical vibrations causes bulk changes in the magnetization of the material due to the rotation of the magnetic domains and domain wall motion [5]. Among giant magnetostrictive materials, galfenol is considered more suitable for energy harvesting applications as compared to Terfenol-D. The characteristics of galfenol include strong magneto-elastic coupling, ductile nature, low hysteresis losses, moderate magnetostriction (~250–350 ppm) at low magnetic fields (~10 kA/m) and high tensile strength (~500 MPa). In addition, due to its steel-like structural properties, galfenol can be welded, rolled and machined easily. On the other hand, Terfenol-D shows large magnetostriction (~1200–1600 ppm) at a high saturation magnetization (~160 kA/m), but it is quite brittle in nature having low tensile stress and poor machinability [6].

\*Corresponding author: Umair Ahmed  
Email address: umair.ahmed@tuni.fi

Moreover, the magnetostrictive properties of galfenol have been analyzed in [7]–[10]. Galfenol offers a strong coupling coefficient as compared to Terfenol-D [7] and demonstrates large magnetostriction at a wide range of temperatures, showing weak temperature dependence [8]. Stress annealing changes the magnetostriction of galfenol and full magnetostriction can be achieved even at zero prestress [9]. The effect of change in Young's modulus  $\Delta E$  is studied in [10] by applying a static compressive load from 0.5–63.3 MPa. In addition, the results from [11] show that under no applied bias, the Young's modulus varies between 72–78 GPa when the compressive stress ranges from 15–60 MPa.

Modeling tools are required to investigate the coupled magneto-mechanical effects for a magnetostrictive energy harvester. Furthermore, to optimize the design characteristics of the harvester, modeling tools determine the appropriate design characteristics and operating conditions in order to obtain maximum output power and higher efficiency. The design characteristic includes determining the geometry of the harvester, mechanical preload, amplitude and frequency of mechanical vibrations and magnetic bias. Moreover, the design parameters of the harvester are governed by the available mechanical excitation and are influenced by the physical dimensions, emphasizing the need to develop a model enabling efficient design.

Various models have been developed analyzing coupled magneto-mechanical behavior under uniaxial and multiaxial loading cases [12]–[14]. An axisymmetric finite element model based on Maxwell's and Navier's equations coupled using nonlinear magnetomechanical constitutive laws is discussed in [13]. A Helmholtz free energy density based magneto-mechanical model utilizing thermodynamic approach has been proposed in [14]. The former utilizes the magnetic field and stress as the state variables, which requires numerically inverting the constitutive model when using it in finite element (FE) formulations based on the magnetic vector potential and mechanical displacement. On the other hand, the latter utilizes magnetic flux density and strain as state variables, and can be directly applied in FE tools. In addition, a magnetic hysteresis model due to applied bias and mechanical stress is presented in [15]. The model is based on analytical expressions for domain rotation, accurately describing the non-linear magnetization vs. field and strain vs. stress behavior in the dominant domain rotation regions. However, the models presented in [12], [14], [15] have not yet been applied for analysing prototype magneto-mechanical transducers to be employed for harvesting energy.

Fully coupled nonlinear magneto-elastic models for magnetostrictive transducers are presented in [16]–[18]. Taking into account the nonlinear and dynamic behavior of magnetostrictive materials, the approach in [16] utilizes the Armstrong model representing an energy-based magneto-mechanical constitutive law, whereas [17] presents a class of phenomenological models for magneto-elastic interactions in materials with losses due to hysteresis. The model in [18] is based on constitutive equations resembling piezoelectricity. Models analyzing a magnetostrictive energy harvesting

concept device are presented in [19]–[21]. A Preisach based phenomenological model for the analysis of optimization problems for harvesters is presented in [19]. A Gibbs free energy based fully coupled model for analyzing a magnetostrictive energy harvester concept device is discussed in [20]. The approach utilizes a three port equivalent circuit model related to mechanical, magnetic and electrical parts of a concept energy harvester, to be implemented in circuit simulation software.

In this paper, we apply a thermodynamic free energy density approach presented in [14] to analyze a galfenol-based magnetostrictive energy-harvesting concept device for the first time. The loss due to hysteresis for galfenol is small [21] and thus excluded from the analysis. We first present an analytical energy density function for expressing the coupled magneto-mechanical constitutive law. The model parameters are then determined by fitting the analytical energy density function against measured magnetization curves. The Maxwell and mechanical balance equations are solved utilizing the constitutive law in an axisymmetric FE model. Finally, measurements from a prototype energy harvesting concept device are compared with the simulated results to validate the model.

## 2. Experimental setup and working principle

### 2.1. Material characterization

First, the characterization of the galfenol rod ( $\text{Fe}_{81.6}\text{Ga}_{18.4}$ ) used in the prototype concept device was carried out for identifying the constitutive law. The schematic diagram of the experimental setup for the characterization of the material is presented in Fig. 1. The key components of the setup include the galfenol rod, magnetizing coils, a U-shaped magnetic core, a Hall probe and a prestress mechanism. The galfenol rod has a length of 60 mm with a diameter of 12 mm. The overall dimensions of the U-shaped magnetic core are 120 mm x 68 mm x 15 mm. The magnetizing coils are connected in series, consist of 600 turns, and are able to supply current up to 6 A through a power amplifier.

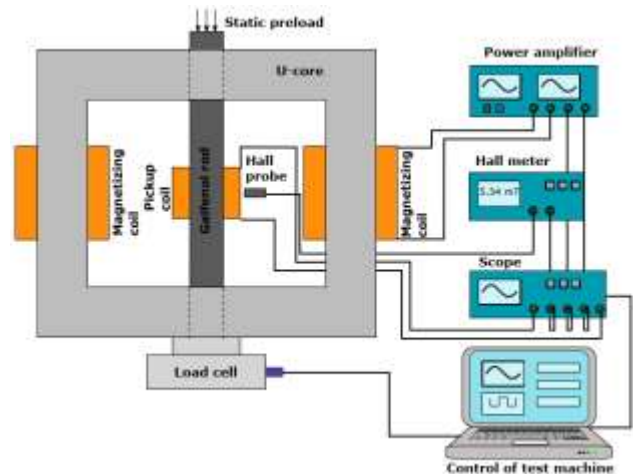


**Fig. 1.** Schematic diagram of the measurement system for the characterization of the magnetostrictive material.

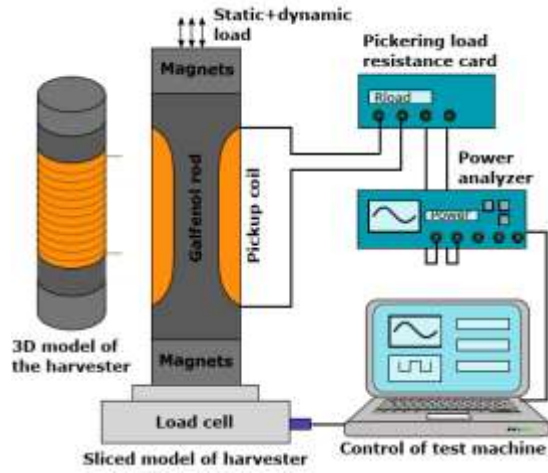


**Fig. 2.** Schematic diagram of the measurement system for the concept energy harvester and internal structure of the concept device (sliced model).

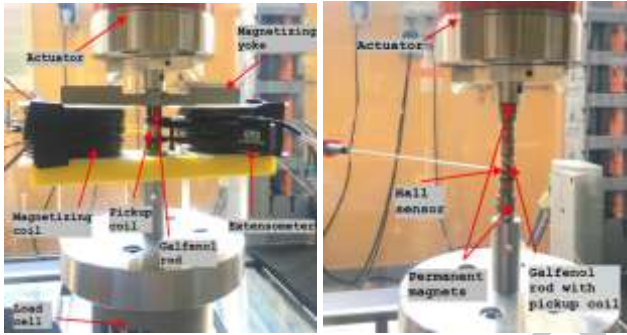


**Fig. 3.** Actual setup for the material characterization (left) and energy harvester concept device (right).

A static axial compressive prestress (preload)  $\sigma$  was first applied using a high performance test machine (Instron ElectroPuls E10000) in force control mode. The galfenol rod was then magnetized by supplying a 200 mHz AC voltage to the magnetizing coils using a signal generator and a power amplifier. The longitudinal strain  $\varepsilon$  was measured using an extensometer clamped in the middle of the sample. Finally, the magnetic field strength  $H$  was measured by a Hall probe placed in contact with the middle part of the sample and the average flux density  $B$  was obtained by integrating the induced voltage from the pickup coil wound around the active material. The measured magnetization and magnetostriction curves were obtained at different compressive preload values ranging from 0 to 80 MPa.

## 2.2. Energy harvester

The schematic diagram for the prototype harvester concept device is presented in Fig. 2 (right). The device consists of a galfenol rod utilized as an active material and two permanent magnets. The galfenol rod is machined as shown in the Fig. 2 (left) with a diameter of 6 mm in the middle and 12 mm from both ends to accommodate the pickup coil. The pickup coil consists of 2000 turns wound from 0.02 mm thick copper wire. The actual experimental setup is presented in Fig. 3

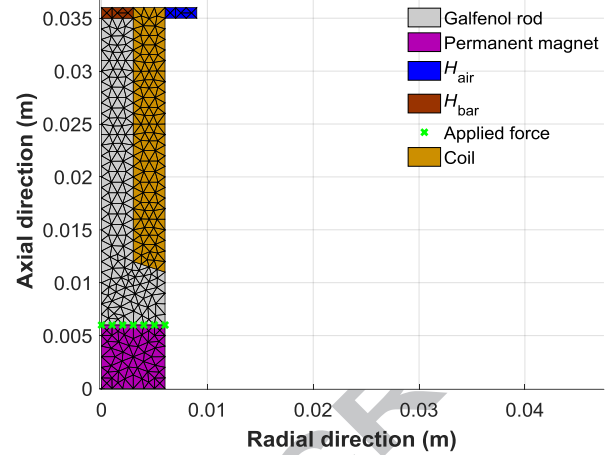


**Fig. 4.** Geometry and FE mesh of the prototype harvesters' concept device used in the axisymmetric magneto-mechanical FE model. The markers denote the nodes where the force is applied. Due to symmetry, only one half of the geometry is modeled.

whereas, the geometry and FE mesh of the prototype harvester device used in the axisymmetric magneto-mechanical FE model are presented in Fig. 4. The markers in Fig. 4 denote the nodes where the axial force is applied. The regions marked as  $H_{air}$  and  $H_{bar}$  are used for computing the magnetic field in the air and inside the galfenol bar based on the FE solution. This is further discussed in Sections 3.2 and 4.2.

A constant magnetic bias is applied using two NdFeB magnets having a remanence flux density  $B_r = 1.13$  T and coercive field  $H_c = 955$  kA/m with physical dimensions of 6 mm in thickness and 12 mm in diameter. The magnets are attached at both ends of the galfenol rod and the axial load is applied through the magnets as shown in Fig. 2. The NdFeB magnets are coated with a phosphate coating. This is the treatment for the magnets used in actuators, which is particularly suitable to protect magnets from the effects of mechanical stress. After an intense stress, the properties of the magnets remain unaltered, provided that the stress is applied gradually, as it occurs in the compression machine. A dynamic compressive stress is applied on the bar in the axial direction using a force actuator, which is capable of providing a static offset force (preload) and a sinusoidal vibrational force up to 100 Hz frequency and 10 kN in amplitude.

The vibrational force is measured by a load cell with an expanded uncertainty  $\leq 0.5\%$ . The harvester is first subjected to a static preload followed by a dynamic load at three different amplitudes (4, 6 and 8 MPa). The dynamic load is applied at a frequency of 100 Hz. The experimental procedure is then repeated for different preload values ranging from 40 to 80 MPa with an increment of 5 MPa. The voltage induced into the pickup coil as a result of the Villari effect and Faraday's law is measured using a precision power analyzer (Yokogawa WT3000). A Pickering programmable precision resistor (1%) card PXI 40-297-002, controlled by LabVIEW software, measures the output power. The programmable load

resistance is varied to determine the maximum output power from the prototype concept device at different preload and dynamic load values. In this study, we analyze the effect of preload and dynamic load on the harvester, keeping the magnetic bias constant.

### 3. Models

#### 3.1. Constitutive model

The energy harvester is modeled using a thermodynamic approach based on the Helmholtz free energy density function  $\psi(\mathbf{B}, \boldsymbol{\varepsilon})$  presented in [14], where the state variables are the magnetic flux density vector  $\mathbf{B}$  and the strain tensor  $\boldsymbol{\varepsilon}$ . The total strain  $\boldsymbol{\varepsilon} = \mathbf{C}^{-1}\boldsymbol{\sigma} + \boldsymbol{\lambda}$  includes both the mechanical strain  $\mathbf{C}^{-1}\boldsymbol{\sigma}$  and the strain caused by magnetostriction  $\boldsymbol{\lambda}$ , where  $\mathbf{C}$  is the mechanical stiffness matrix and  $\boldsymbol{\sigma}$  the stress. The state variables can be written in terms of six scalar invariants as

$$I_1 = \text{tr } \boldsymbol{\varepsilon}, I_2 = \text{tr } \boldsymbol{\varepsilon}^2, I_3 = \text{tr } \boldsymbol{\varepsilon}^3, \quad (1)$$

$$I_4 = \frac{\mathbf{B} \cdot \mathbf{B}}{B_{\text{ref}}^2}, I_5 = \frac{\mathbf{B} \cdot \mathbf{eB}}{B_{\text{ref}}^2}, I_6 = \frac{\mathbf{B} \cdot \mathbf{e}^2 \mathbf{B}}{B_{\text{ref}}^2},$$

where  $\text{tr}$  denotes the trace of a tensor,  $\mathbf{e}$  represents the deviatoric strain given by  $\mathbf{e} = \boldsymbol{\varepsilon} - \frac{1}{3}(\text{tr } \boldsymbol{\varepsilon})\mathbf{I}$ , and  $\mathbf{I}$  is the second-order identity tensor.  $B_{\text{ref}} = 1 \text{ T}$  is only used for scaling purposes to make the invariants dimensionless. The Helmholtz free energy density, describing the magneto-mechanical interaction in the actuator material, is then written as

$$\psi = \frac{1}{2}\lambda I_1^2 + \mu I_2 + \sum_{i=1}^{n_\alpha} \alpha_i I_4^i + \sum_{i=1}^{n_\beta} \beta_i I_5^i + \sum_{i=1}^{n_\gamma} \gamma_i I_6^i, \quad (2)$$

where the polynomial coefficients  $\alpha_i$ ,  $\beta_i$  and  $\gamma_i$  are parameters fitted against the  $B$ - $H$  curves obtained from the characterization measurements discussed in Section 2.1, and  $\lambda$  and  $\mu$  are the Lamé parameters obtained from Young's modulus and Poisson's ratio for an isotropic material. The first two invariants  $I_1$  and  $I_2$  are related to pure mechanical behavior. The invariant  $I_3$  is not utilized considering linear elastic behavior.  $I_4$  is related to purely magnetic behavior, whereas  $I_5$  and  $I_6$  describe the magneto-elastic behavior.

The constitutive equations for the magnetic field strength  $\mathbf{H}$  and the Cauchy stress tensor  $\boldsymbol{\sigma}$ , considering an isotropic ferromagnetic material, are obtained by computing the partial derivatives of  $\psi$  with respect to  $\mathbf{B}$  and  $\boldsymbol{\varepsilon}$  as

$$\mathbf{H}(\mathbf{B}, \boldsymbol{\varepsilon}) = \left( \frac{\partial \psi}{\partial \mathbf{B}} \right)^T \text{ and } \boldsymbol{\sigma}(\mathbf{B}, \boldsymbol{\varepsilon}) = \frac{\partial \psi}{\partial \boldsymbol{\varepsilon}}, \quad (3)$$

where  $T$  denotes the transpose.

#### 3.2. Finite element model

In the actuator material, the axisymmetric magneto-mechanical FE model is based on solving the mechanical

balance equations and the combination of Ampere's and Faraday's laws:

$$\nabla \cdot \boldsymbol{\sigma}(\mathbf{B}, \boldsymbol{\varepsilon}) = 0, \quad (4)$$

$$\nabla \times \mathbf{H}(\mathbf{B}, \boldsymbol{\varepsilon}) + \kappa \frac{\partial \mathbf{A}}{\partial t} = 0, \quad (5)$$

where  $\kappa$  is the electrical conductivity. The circumferential magnetic vector potential  $\mathbf{A} = A\mathbf{e}_\theta$ , and the displacement vector  $\mathbf{u} = u_r\mathbf{e}_r + u_z\mathbf{e}_z$  in the symmetry plane are used as the field variables, from which the flux density and strain are obtained as  $\mathbf{B} = \nabla \times \mathbf{A}$  and  $\boldsymbol{\varepsilon} = (\nabla \mathbf{u} + (\nabla \mathbf{u})^T)/2$ . Equations (4) and (5) are coupled through the constitutive law (2) and (3). In other regions with constant magnetic reluctivity  $\nu$ , only the electromagnetic problem

$$\nu \nabla \times \nabla \times \mathbf{A} + \kappa \frac{\partial \mathbf{A}}{\partial t} = \mathbf{J}_s + \nabla \times \mathbf{H}_c, \quad (6)$$

is solved.  $\mathbf{J}_s = (Ni_{\text{coil}}/S_{\text{coil}})\mathbf{e}_\theta$  is the circumferential source current density, which is nonzero only in the pickup coil with  $N$  turns, cross-sectional area  $S_{\text{coil}}$  and current  $i_{\text{coil}}$ , while  $\kappa$  and  $\mathbf{H}_c = H_c\mathbf{e}_z$  are the electrical conductivity and axially-oriented coercive field respectively, which are nonzero only in the permanent magnets.

The field problem and the variables  $A$ ,  $u_r$  and  $u_z$  are discretized using a standard Galerkin FE discretization with nodal shape functions  $\mathbf{N} = [N_1, N_2, \dots]$ . The current  $i_{\text{coil}}$  of the pickup coil is set as an additional variable to be solved from a voltage equation, assuming the coil to have an internal resistance  $R$  and to be connected to a load resistance  $R_{\text{load}}$ . The complete system of equations is

$$\begin{aligned} & \int_{\Omega} r \left( - \left( \frac{\partial \mathbf{N}^T}{\partial r} + \frac{\mathbf{N}^T}{r} \right) H_z + \frac{\partial \mathbf{N}^T}{\partial z} H_r \right) d\Omega \\ & + \left( \int_{\Omega} r \kappa \mathbf{N}^T \mathbf{N} d\Omega \right) \frac{da}{dt} - \mathbf{D}i_{\text{coil}} = 0, \\ & \int_{\Omega} r \left( \frac{\partial \mathbf{N}^T}{\partial r} \boldsymbol{\sigma}_r + \frac{\partial \mathbf{N}^T}{\partial z} \boldsymbol{\sigma}_z \right) d\Omega + \int_{\Gamma} r \mathbf{N}^T [\boldsymbol{\sigma}_r \ \boldsymbol{\sigma}_z] \mathbf{n} d\Gamma = 0, \quad (7) \\ & \int_{\Omega} r \left( \frac{\partial \mathbf{N}^T}{\partial r} \boldsymbol{\sigma}_r + \frac{\mathbf{N}^T}{r} \boldsymbol{\sigma}_{\theta\theta} + \frac{\partial \mathbf{N}^T}{\partial z} \boldsymbol{\sigma}_{zz} \right) d\Omega \\ & + \int_{\Gamma} r \mathbf{N}^T [\boldsymbol{\sigma}_r \ \boldsymbol{\sigma}_{zz}] \mathbf{n} d\Gamma = 0, \\ & \mathbf{C} \frac{da}{dt} + (R + R_{\text{load}})i_{\text{coil}} = 0, \end{aligned}$$

where  $r$  denotes the radial coordinate and the vector  $\mathbf{a}$  contains the nodal values of the vector potential,  $A = \mathbf{N}\mathbf{a}$ . Furthermore,  $\boldsymbol{\sigma}_r$ ,  $\boldsymbol{\sigma}_{zz}$ ,  $\boldsymbol{\sigma}_{\theta\theta}$ ,  $H_r$  and  $H_z$  are the radial ( $r$ ), axial ( $z$ ) and circumferential ( $\theta$ ) components of the stress and the magnetic field strength, respectively. In addition,  $\Omega$  denotes the calculation domain in the axisymmetric plane,  $\Gamma$  the boundary lines inside  $\Omega$  where the mechanical loading is applied, and  $\mathbf{n}$

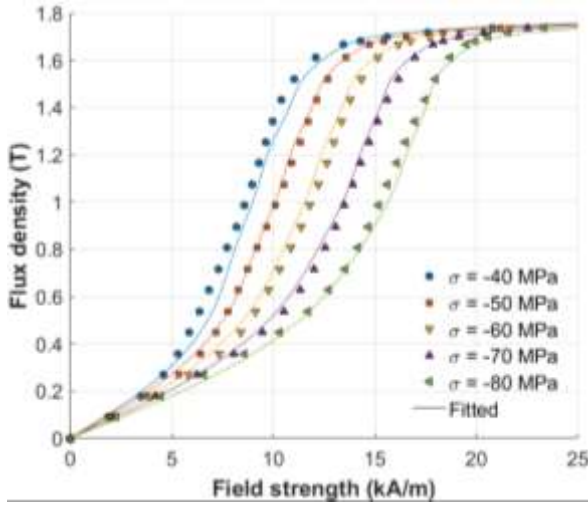


**Fig. 5.** Measured and fitted magnetization curves under different values of static compressive stress.

the outer normal vector of  $\Gamma$ . The winding matrices related to the flux linkage  $C$  and source current density  $D$  are given by,

$$C = \frac{2\pi N}{S_{\text{coil}}} \int_{\Omega_{\text{coil}}} r N d\Omega, \quad (8)$$

$$D = \frac{N}{S_{\text{coil}}} \int_{\Omega_{\text{coil}}} r N^T d\Omega.$$

As boundary conditions,  $A$  is fixed to zero at the outer boundaries, and radial displacement  $u_r$  and axial displacement  $u_z$  are fixed to zero at the longitudinal middle axis and in the middle cross-section of the actuator, respectively. The time-derivatives are discretized using the Backward-Euler method,

$$\frac{da}{dt} = \frac{a - a_{\text{prev}}}{\Delta t}, \quad (9)$$

where  $\Delta t$  is the time step which is chosen to be 100  $\mu\text{s}$ , and the discretized system (7) is solved with the Newton-Raphson method.

## 4. Results

### 4.1 Fitting of the constitutive model

The measured magnetization curves and their fitting to the analytical expression (2) under various static compressive loadings are presented in Fig. 5. The measured results are plotted as single valued  $B$ - $H$  curves by taking the mean value of the hysteresis loop. It is worthwhile to note that galfenol shows negligible hysteresis and a small coercive field, which means lower energy conversion losses as compared to Terfenol-D [20], [22]. Therefore, taking the mean value of the hysteresis loop does not significantly affect the accuracy of the solution. The result shows that the permeability of the material decreases due to applied compressive stress. In addition, the

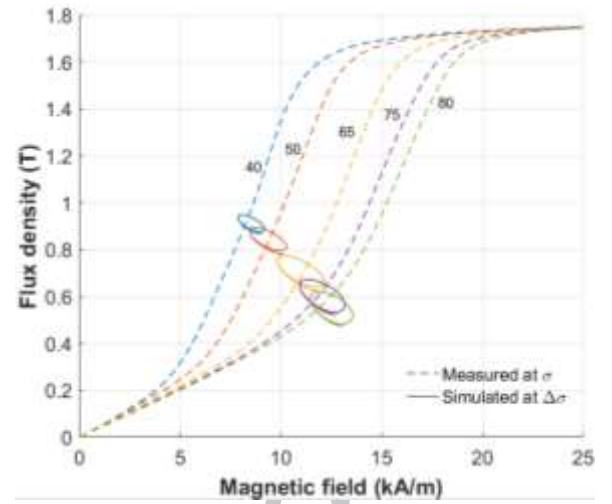


**Fig. 6.** Measured magnetization curves obtained during characterization at various compressive preload ( $\sigma$ ) values and simulated dynamic hysteresis loops under cyclic loading ( $\Delta\sigma$ ) of 8MPa.

fitted curves accurately correspond to the measured curves. The percentage differences between measured and simulated field strengths are 17.94% for 40 MPa, 4.76% for 50 MPa, 8.83% for 60 MPa, 4.09% for 70 MPa and 7.45% for 80 MPa preload values. The values of the fitting parameters for  $\alpha_i$ ,  $\beta_i$  and  $\gamma_i$  when  $n_\alpha = 11$ ,  $n_\beta = 1$  and  $n_\gamma = 2$  are given in Table I. The values for Young's modulus and Poisson's ratio utilized during simulation are 75 GPa and 0.4 respectively.

**Table 1.** Coefficients of the model parameters

Parameter	Value (J/m <sup>3</sup> )	Parameter	Value (J/m <sup>3</sup> )
$\alpha_1$	$9.217 \times 10^3$	$\alpha_8$	$-1.071 \times 10^4$
$\alpha_2$	$-1.208 \times 10^4$	$\alpha_9$	$2.754 \times 10^3$
$\alpha_3$	$1.854 \times 10^4$	$\alpha_{10}$	-399.5
$\alpha_4$	$-3.159 \times 10^4$	$\alpha_{11}$	24.99
$\alpha_5$	$4.286 \times 10^4$	$\beta_1$	$4.647 \times 10^6$
$\alpha_6$	$-4.082 \times 10^4$	$\gamma_1$	$1.128 \times 10^{10}$
$\alpha_7$	$2.595 \times 10^4$	$\gamma_2$	$-6.977 \times 10^5$

### 4.2 Finite element simulations

The measured magnetization curves are utilized in FE simulations of the prototype harvester concept device to compute the change in the magnetic flux density ( $\Delta B$ ) inside the sample under cyclic mechanical loading.  $\Delta B$  and the corresponding magnetic fields are averaged over the region  $H_{\text{bar}}$  shown in Fig. 4. The measurement results of the magnetization curves under static preload (40–80 MPa) and simulated results of  $\Delta B$  upon static loading (40–80 MPa) followed by a dynamic cyclic loading ( $\Delta\sigma$ ) of 8 MPa at 100 Hz frequency are presented in Fig. 6. The  $\Delta B$  upon mechanical vibration is plotted as hysteresis loops representing the operating points of  $B$ . The simulated results

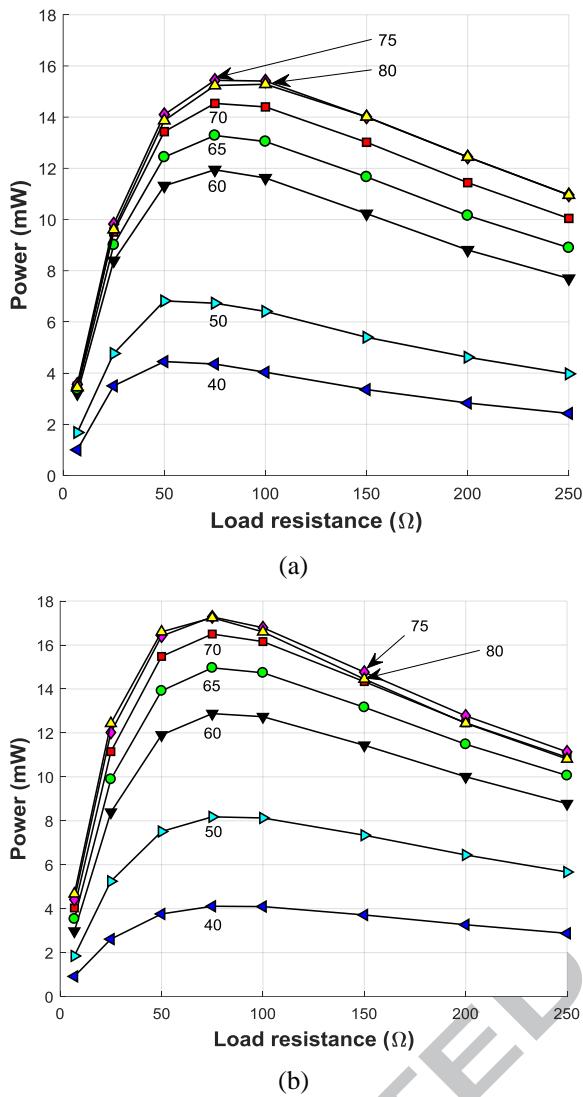


**Fig. 7.** Comparison among measured (a) and simulated (b) average power under constant dynamic load (8 MPa) and changing preload ( $\sigma$ ).

of  $\Delta B$  help to analyze and determine the optimal preload value. Both measurements and simulations were performed using preload values ranging from 0–80 MPa. However, not all of the  $B$ - $H$  curves are plotted, in order to avoid overlapping and to clearly demonstrate the effect of preload upon magnetic flux density. The results in Fig. 6 depict change in the  $\Delta B$  for different values of preload, which is shown by the area of the hysteresis loops. Such an area represents the average power at the corresponding preload case. A large area means a large  $\Delta B$  value, which will generate higher power.

In order to validate the proposed axisymmetric FE model, the measurements for the average output power from the concept harvester setup are compared with the simulation results. The comparison between the measured and simulated average power is given in Fig. 7 (a) and (b) respectively, under a constant dynamic load of 8 MPa and using seven different preload cases ranging from 40 to 80 MPa.

The time step length of  $\Delta t = 100 \mu\text{s}$  (100 steps per one fundamental period) of the 100 Hz mechanical loading, was

considered suitable providing reasonable accuracy of the solution. A magnetostatic solution was used as the initial state, and three fundamental periods were simulated to ensure steady state. The simulations take approximately 130 ms per one time step, independently of the used time step ( $\Delta t$ ). Various time step lengths were tested for the 56 simulations shown in Fig. 7 (b), and the total computation time for all simulations and the percentage difference of the output power with respect to the  $\Delta t = 100 \mu\text{s}$  case were compared. The results for the comparison are presented in Table 2.

**Table 2.** Simulation times and output power differences for different step sizes (for the 56 simulations in Fig. 7 (b))

Time step $\Delta t$ ( $\mu\text{s}$ )	Total simulation time (min)	Power difference w.r.t. $\Delta t = 100 \mu\text{s}$ (%)
200	20	-2.7 %
100	36	0 %
50	72	1.5 %
33	86	1.9 %
25	133	2.2 %
20	165	2.4 %
12.5	188	2.5 %

The results from the table show that reducing the time step down to  $\Delta t = 12.5 \mu\text{s}$  the output power increases by 2.5 % compared to the  $\Delta t = 100 \mu\text{s}$  case at the additional computational cost of 152 minutes. On the other hand, increasing the time step to  $\Delta t = 200 \mu\text{s}$  the output power decreases by 2.7 %, saving 14 minutes. Thus, the step size of  $100 \mu\text{s}$  resulted to be a good compromise between the accuracy of the solution and the computation time.

The repeatability of the measurements is crucial to obtain accurate results. For this reason, three consecutive tests were conducted without perturbing the external conditions and the output power was recorded carefully each time. The measurement results in Fig. 7 (a) are thus plotted as the average of three repeatedly done experiments. The measured results from Fig. 7 (a) show that the output power increases with the increase in the preload, reaches its maximum at 75 MPa, and then starts decreasing gradually. The same phenomenon is also predicted by the simulated results in Fig. 7 (b), but with slightly higher amplitudes.

This increase in power is due to the change in the flux density variation  $\Delta B$  with the increase of preload. The flux density variation reaches its maximum value around 75 MPa, which is also evident from the area of the hysteresis loops in Fig. 6. The  $\Delta B$  at 75 and 80 MPa preload under dynamic load of 8 MPa is computed as 152.7 and 147.2 mT respectively. Furthermore, the output power is given as a function of the load resistance. The load resistance is varied in order to determine its optimal value at which maximum power can be obtained. In both the measurements and simulations, the optimal load resistance remains constant at 75  $\Omega$ .

In addition, some differences in the measured output power for the three repeatedly performed experiments were

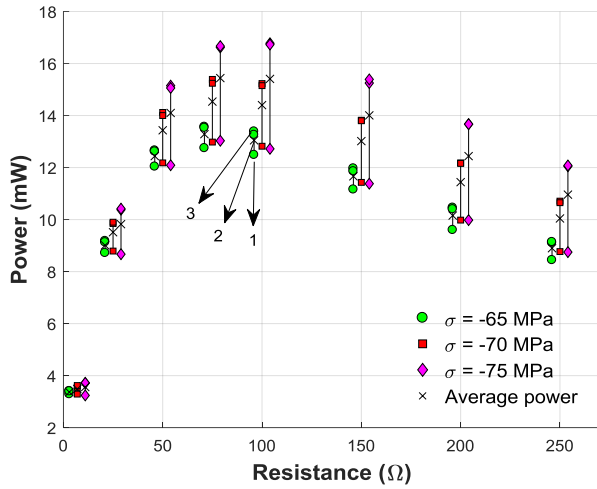


**Fig. 8.** Output powers obtained from the three separate measurement sessions (1, 2 and 3). The markers denote the measured output powers from each session. The crosses denote the average values, i.e., the results presented in Fig. 7 (a). The -65 MPa and -75 MPa markers have been shifted horizontally for clarity, but the resistance values are the same for each preload.

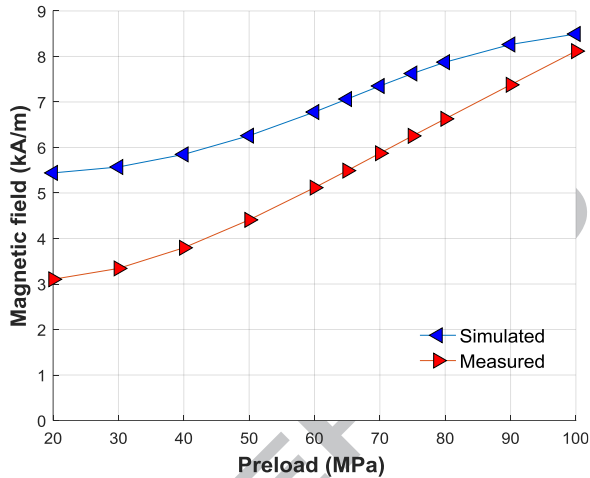


**Fig. 9.** Comparison among measured and simulated magnetic field intensity  $H$  (average values) near the middle part of the sample for different preload values under constant dynamic load (8 MPa).

observed without perturbing the external conditions. The output powers for the separate sessions (1, 2 and 3) are presented in Fig. 8. The average power is presented as crosses, which corresponds to the measurement results shown in Fig. 7 (a) for three different loading cases (-65, -70 and -75 MPa). It was observed that, in the first session, a lower output power is obtained compared to second and third sessions which are nearly coincident, which shows the sensitivity of the measurements to the external conditions. In addition, variability between single experiments increases with the preload. The maximum percentage difference between the variations of the measurements vs. the average output power

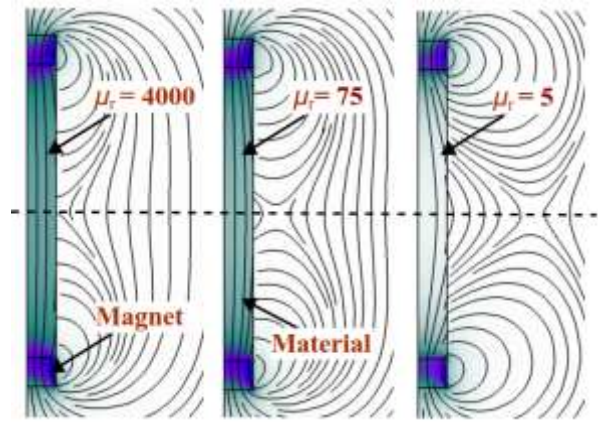


**Fig. 10.** Simulated field lines of magnetic flux density around a rectangular material sample magnetized by two permanent magnets at both ends at three different values of relative permeability ( $\mu_r$ ). The dashed line represents the area of interest where  $B$  is computed.

at 65 MPa is lower than 10%, at 70 MPa is lower than 20% and at 75 MPa reaches 30% respectively. We are mostly interested in the higher stress range values, thus, the selection of (65–80 MPa) preload and dynamic load (8 MPa) is made considering the specific range of prestress values yielding maximum output power. Moreover, it was observed that even a minor misalignment of the sample also affects the repeatability of the measurements.

The comparison among measured and simulated field strength  $H$  in the air near the middle part of the sample (region  $H_{\text{air}}$  in Fig. 3) is presented in Fig. 9. Both the measurements and simulations show an increasing  $H$  under increasing compression. This can be explained by the illustration presented in Fig. 10, where a simplified sample with relative permeability  $\mu_r$  is placed between two permanent magnets. As  $\mu_r$  is decreased (from the left to the right in Fig. 10), a larger share of the total flux is forced into the air, which is seen in the bending flux lines near the middle part of the sample indicated by the dashed line. The same happens when the permeability of the sample decreases due to an increase in compression. Fig. 9 also shows that the simulated magnetic field is overestimated as compared to measured one, and that the difference reduces when compression increases. This is due to the fact that the model slightly underestimates the permeability of the sample for lower values of stress, like seen in the -40 MPa curve in Fig. 5. Comparison among the measured and simulated average power, presented in Fig. 7, should be evaluated keeping in view the limitations of the model, the sensitivity of the measurements and their repeatability.

Now, in order to validate the optimal preload value of 75 MPa suggested by Fig. 7 (a) and (b), simulations were conducted at a wider range of preload values (20 to 110 MPa) to clearly see the effect of the preload on the output power. The results of the mean value of  $B$  inside the bar computed at region  $H_{\text{bar}}$  from Fig. 4 and the average output power vs.  $H$  at

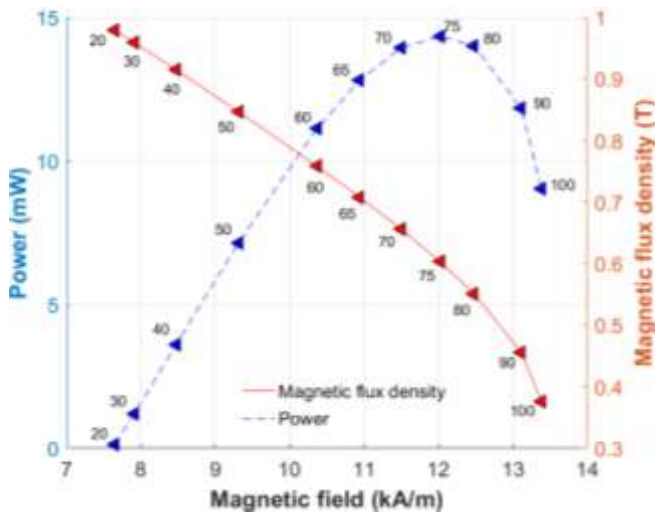


**Fig. 11.** Simulated results for the mean value of magnetic flux density inside the bar and average output power under various prestress values at dynamic load of 8 MPa, using 75  $\Omega$  as load resistance.

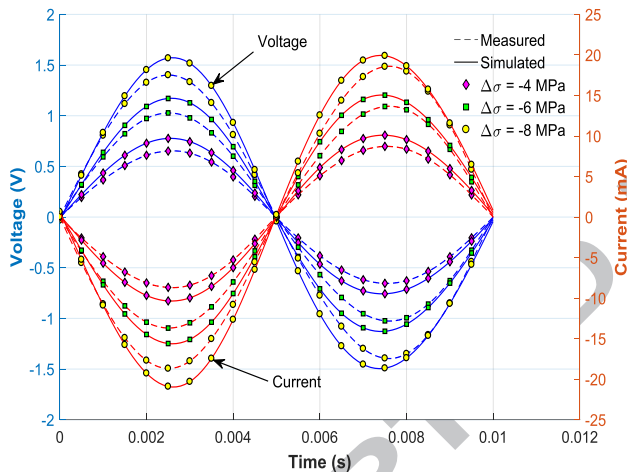


**Fig. 12.** Measured and simulated voltage and current waveforms under a constant preload (65 MPa) and a changing dynamic load using a constant load resistance of 75  $\Omega$ .

preload ranging from 20 to 110 MPa are presented in Fig. 11. The simulation is done using a dynamic load of 8 MPa together with the optimal load resistance value of 75  $\Omega$  yielding the maximum power. The results from Fig. 11 also evidence an increase in the output power, reaching its maximum at 75 MPa, and then decreasing upon further increase in the preload.

The comparison of measured and simulated waveforms of the current and voltage at the optimal load resistance value of 75  $\Omega$  under a constant preload of 65 MPa and a changing dynamic load (6–8 MPa) is presented in Fig. 12. As expected, the measured and simulated results evidence an increase of the induced voltage and current under an increase in the amplitude of the dynamic cyclic load. This validates the fact that the output power is directly proportional to the increase in the

amplitude of mechanical vibrations [22]. In addition, the simulated results of voltage and current are in quite a good agreement with the measured results, following the trend reasonably, which also validates the modeling approach.

## 5. Discussion and conclusion

An axisymmetric FE model utilizing a thermodynamic approach was presented in this paper to analyze the magneto-mechanical behavior of a magnetostrictive energy harvester concept device. A comparison between measured and simulated results was carried out to validate the proposed modeling approach. The comparison showed that the model can predict the simulated values of power, voltage and current with reasonable accuracy, and accurately follows the trend of the measurement results.

The measurements under dynamic loading were found quite sensitive to changes in external parameters, including the warm-up time for the harvester device, the displacement of permanent magnets, and the alignment of the harvester with respect to the vertical loading system. These parameters should be kept constant to ensure reproducibility in the measured results. Therefore, the measured values were taken as the average of repeated readings for three consecutive experiments in order to compensate for some variability in the measurements. The difference in the measured and simulated results is in part due to limitations of the model and the lack of repeatability of the measurements, as indicated in Fig. 8. Furthermore, some of the difference between the measured and simulated values also occurs because the model overestimates the relative permeability of the material, as discussed in Section 4.2.

In this study, we are mainly interested in the prestress range that maximizes the output power. It was observed that the measured and simulated power for the preload values ranging from 65–80 MPa better match each other, following the trend reasonably, with slightly higher amplitudes for the simulated values. In addition, the maximum output power is a function of preload and load resistance. Therefore, load resistance is varied to obtain an optimal value that results in maximum power. The FE model enabled us to compute the magnetic flux density inside the sample, which is not possible to measure physically. The results presented in Fig. 11 provide insight into how the permeability of the material changes under applied compressive preload, as well as its influence on the output power. Given the general agreement between calculated and simulated results, the device behavior for preloads greater than 80 MPa has been extrapolated using the numerical model. The simulated results for the preload ranging from 20 to 110 MPa suggest that the maximum power can only be obtained at a certain preload value (75 MPa) and a certain magnetic field bias that serve as design characteristics. The proposed modeling approach can thus be applied to analyze a magneto-mechanical energy harvester and determine the optimal design characteristics and operating conditions.

## Acknowledgement

This work was supported by the Academy of Finland (304112).

## References

- [1] Dapino, M.J., 2004. On magnetostrictive materials and their use in adaptive structures. *Structural Engineering and Mechanics*, 17(3–4), pp.303–330.
- [2] Zhang, T., Jiang, C., Zhang, H. and Xu, H., 2004. Giant magnetostrictive actuators for active vibration control. *Smart materials and structures*, 13(3), p.473.
- [3] Fiorillo, F., “Measurements of Magnetic Materials,” *Metrologia*, vol. 47, no. 2, 2010: S114.
- [4] Davino, D., Giustiniani, A. and Visone, C., 2009. Capacitive load effects on a magnetostrictive fully coupled energy harvesting device. *IEEE Transactions on Magnetics*, 45(10), pp.4108–4111.
- [5] Atulasimha, J. and Flatau, A.B., 2011. A review of magnetostrictive iron–gallium alloys. *Smart Materials and Structures*, 20(4), p.043001.
- [6] Berbyuk, V., 2013, April. Vibration energy harvesting using Galfenol-based transducer. In *Active and Passive Smart Structures and Integrated Systems 2013* (Vol. 8688, p. 86881F). International Society for Optics and Photonics.
- [7] Kellogg, R.A., Flatau, A.B., Clark, A.E., Wun-Fogle, M. and Lograsso, T.A., 2002. Temperature and stress dependencies of the magnetic and magnetostrictive properties of Fe 0.81 Ga 0.19. *Journal of applied physics*, 91(10), pp.7821–7823.
- [8] Weng, L., Walker, T., Deng, Z., Dapino, M.J. and Wang, B., 2013. Major and minor stress-magnetization loops in textured polycrystalline Fe 81.6 Ga 18.4 Galfenol. *Journal of Applied Physics*, 113(2), p.024508.
- [9] J Yoo, J.H., Pelligrini, G., Datta, S. and Flatau, A.B., 2011. An examination of Galfenol mechanical–magnetic coupling coefficients. *Smart Materials and Structures*, 20(7), p.075008.
- [10] Wun-Fogle, M., Restorff, J.B., Clark, A.E., Dreyer, E. and Summers, E., 2005. Stress annealing of Fe–Ga transduction alloys for operation under tension and compression. *Journal of applied physics*, 97(10), p.10M301.
- [11] Bellotti, R., Mei, P., Picotto, G., Santiano, M. and Zucca, M., 2017. Strain measurements of cylinder magnetostrictive samples by interferometer readings. In *17th International EUSPEN Conference & Exhibition* (No. P6. 19, pp. 379–380). EUSPEN.
- [12] Daniel, L., Hubert, O. and Rekik, M., 2015. A simplified 3-D constitutive law for magnetomechanical behavior. *IEEE Transactions on Magnetics*, 51(3), pp.1–4.
- [13] Chakrabarti, S. and Dapino, M.J., 2012. Coupled axisymmetric finite element model of a hydraulically amplified magnetostrictive actuator for active powertrain mounts. *Finite Elements in Analysis and Design*, 60, pp.25–34.
- [14] Fonteyn, K., Belahcen, A., Kouhia, R., Rasilo, P. and Arkkio, A., 2010. FEM for directly coupled magneto-mechanical phenomena in electrical machines. *IEEE Transactions on Magnetics*, 46(8), pp.2923–2926.
- [15] Evans, P.G. and Dapino, M.J., 2010. Efficient magnetic hysteresis model for field and stress application in magnetostrictive Galfenol. *Journal of Applied Physics*, 107(6), p.063906.
- [16] Graham, F.C., Mudivarthi, C., Datta, S. and Flatau, A.B., 2009. Modeling of a Galfenol transducer using the bidirectionally coupled magnetoelastic model. *Smart Materials and Structures*, 18(10), p.104013.
- [17] Davino, D., Krejčí, P. and Visone, C., 2013. Fully coupled modeling of magneto-mechanical hysteresis through thermodynamic compatibility. *Smart Materials and Structures*, 22(9), p.095009.
- [18] Pérez-Aparicio, J.L. and Sosa, H., 2004. A continuum three-dimensional, fully coupled, dynamic, non-linear finite element formulation for magnetostrictive materials. *Smart Materials and Structures*, 13(3), p.493.
- [19] Davino, D., Krejčí, P., Pimenov, A., Rachinskii, D. and Visone, C., 2016. Analysis of an operator-differential model for magnetostrictive energy harvesting. *Communications in nonlinear science and numerical simulation*, 39, pp.504–519.
- [20] Clemente, C.S., Mahgoub, A., Davino, D. and Visone, C., 2017. Multiphysics circuit of a magnetostrictive energy harvesting device. *Journal of Intelligent Material Systems and Structures*, 28(17), pp.2317–2330.
- [21] Rezaeealam, B., 2012. Finite element analysis of magnetostrictive vibration energy harvester. *COMPEL-The international journal for computation and mathematics in electrical and electronic engineering*, 31(6), pp.1757–1773.
- [22] Palumbo, S., Rasilo, P. and Zucca, M., 2019. Experimental investigation on a Fe-Ga close yoke vibrational harvester by matching magnetic and mechanical biases. *Journal of Magnetism and Magnetic Materials*, 469, pp.354–363.

**Highlights of the paper**

- An axisymmetric FE model utilizing a thermodynamic approach is presented to analyze energy harvester concept device.
- It provides a simplified approach suitable as a design tool for magnetostrictive harvesters
- Effect of mechanical preload on harvester performances
- The analytical model fits well to the magnetization curves measured under static loading
- Simulated results are validated with measurements following the trends reasonably

ACCEPTED MANUSCRIPT